Sonar-Based Human Leg Localization Using Chaos Enhanced Dynamic Neighborhood Learning-Based GSA Aided sNDT Algorithm

Pritam Paral, Amitava Chatterjee, *Senior Member, IEEE*, Anjan Rakshit, and Sankar K. Pal, *Life Fellow, IEEE*

***Abstract*— The present article proposes a new human leg localization (HLL) algorithm using ultrasonic sensors in human–robot coexisting environments. The algorithm estimates the motion of a human leg pair between two successive sonar scans by using a new *static cluster elimination* (SCE) method, an *edge feature-based leg recognition* algorithm, and an advanced scan matching technique. We also propose a novel, robust approach to overcome *bad initialization* problem in sonar scan matching, by introducing a metaheuristic search (MHS)-based optimization algorithm for the sonar normal distributions transform (sNDT) method. The recently proposed dynamic neighborhood learning-based GSA (DNLGSA) has been successfully utilized in real-life scenario to solve this problem. The work also proposes a new chaos enhanced DNLGSA (CEDNLGSA) to further improve real-life performance and the proposed novel variant of the sNDT method based on CEDNLGSA, called *chaotic MHS-based sNDT* (CMHS-sNDT), has been demonstrated to achieve superior leg detection performance in various real-life case studies, compared to different contemporary state-of-the-art methods.**

***Index Terms*— Chaos enhanced DNLGSA (CEDNLGSA), dynamic neighborhood learning-based GSA (DNLGSA), leg detection, likelihood field (LF), scan matching, sonar sensing.**

NOMENCLATURE

ABC	Artificial bee colony.
ARM	Advanced reduced instruction set computer (RISC) machine.
BFO	Bacterial foraging optimization.
CEDNLGSA	Chaos enhanced dynamic neighborhood learning-based gravitational search algorithm.
CMHS	Chaotic metaheuristic search.
CMHS-sNDT	CMHS-based sonar normal distributions transform.
CoBiDE	Differential evolution based on covariance matrix learning and bimodal distribution parameter setting.
DBSCAN	Density-based spatial clustering of applications with noise.
DD-WMR	Differentially driven wheeled mobile robot.
DE	Differential evolution.
DFSABC_elite	ABC algorithm with depth-first search framework and elite-guided search equation.
DNLGSA	Dynamic neighborhood learning-based gravitational search algorithm.
EFBLR	Edge feature based leg recognition.
EPSO	Ensemble particle swarm optimizer.
FE	Function evaluation.
FOChS	Fractional order chaotic system.
FOChS-PRNG	FOChS-based pseudorandom number generator.
FOVlS	Fractional order Volta's system.
FWS	Forward straddle.
GA	Genetic algorithm.
G-L	Grünwald–Letnikov.
GSA	Gravitational search algorithm.
GWO	Gray wolf optimizer.
HLL	Human leg localization.
HLL-sNDT	HLL with sonar normal distributions transform.
HLL-X-sNDT	HLL with X-based sonar normal distributions transform (X: CMHS, DNLGSA, GWO, CoBiDE, DFSABC_elite, IRDPSO, and EPSO).
HRI	Human–robot interaction.
IRDPSO	Improved random drift particle swarm optimization.
K-S	Kolmogorov–Smirnov.
LF	Likelihood Field.
LPDDR	Low-power double data rate.
LRF	Leg reading frame.
MAE	Mean absolute error.
MHS	Metaheuristic search.
MT-PRNG	Mersenne Twister pseudorandom number generator.
NDT	Normal distributions transform.
NWM	Newton's method.
PRN	Pseudorandom number.

Manuscript received 6 August 2022; revised 18 September 2022; accepted 12 October 2022. Date of publication 25 October 2022; date of current version 8 November 2022. The work of Pritam Paral was supported by the Ministry of Electronics and IT, Government of India through the "Visvesvaraya PhD Scheme for Electronics and IT". The Associate Editor coordinating the review process was Dr. Huang-Chen Lee. *(Corresponding author: Pritam Paral.)*

Pritam Paral and Sankar K. Pal are with the Center for Soft Computing Research, Indian Statistical Institute (ISI), Kolkata 700108, India (e-mail: callinpritam@gmail.com; sankar@isical.ac.in).

Amitava Chatterjee is with the Department of Electrical Engineering, Jadavpur University, Kolkata 700032, India (e-mail: cha_ami@yahoo.co.in).

Anjan Rakshit, retired, was with the Department of Electrical Engineering, Jadavpur University, Kolkata 700032, India (e-mail: anjanrakshit1951@gmail.com).

This article has supplementary downloadable material available at https://doi.org/10.1109/TIM.2022.3216846, provided by the authors.

Digital Object Identifier 10.1109/TIM.2022.3216846

PRNG	PRN generator.
PSO	Particle swarm optimization.
RANSAC/GD	Random sample consensus/Gaussian determination.
RANSAC/GF	Random sample consensus/Gaussian filtering.
RCF	Reading coordinate frame.
RDPSO	Random drift PSO.
RPF	Robot pose frame.
SCE	Static cluster elimination.
SDRAM	Synchronous dynamic random-access memory.
SJM	Short jump.
sNDT	Sonar NDT.
SRCC	Spearman's rank correlation coefficient.
TLA	Two legs apart.
TLT	Two legs together or single leg.
WOA	Whale optimization algorithm.

I. Introduction

OVER the past two decades, HRI has become a rapidly emerging research subject [1], accomplishing objectives like detecting and tracking human supervisors [2], [3], [4], [5], [6], [7], especially using range sensing [5], [6], [7]. The present work proposes a new range sensing-based approach which estimates the motion of the legs of a walking person between two successive time instances, using *scan matching* [8]. Although laser range sensors are known to provide more precise solutions, sonar sensors still continue to offer acceptable alternatives, especially from size, cost and power consumption perspectives, which can be very useful in developing countries.

Among the scan matching algorithms, NDT [9], *probabilistic laser scan registration* [10] approach, and sNDT, a sonar-based variant of NDT [8], are quite popular. In sNDT, *NWM* is utilized to minimize a *score function* [8]. In NWM, the score function should belong to class $\mathbb{C}^1$ (i.e., continuously differentiable) and computation of first- and second-order derivatives in each iteration involve high computational costs. More importantly, NWM's performance degrades if the initial solution is far from the true minimum point. In this work, we propose to overcome this *bad initialization* problem by using metaheuristic-based non-gradient type, global optimization algorithms [11], suited for complex optimization problems. However, determining the global optimum remains a challenging job for MHS-based algorithms [11] too, which requires a judicious balance of *exploration* and *exploitation*.

Some of the popular MHS algorithms include GA, PSO, DE, ABC, BFO, and so on [11]. However, till date, the search for new, improved MHS algorithms remains a hot research topic. For example, Wang et al. [12] proposed CoBiDE, a novel variant of DE based on *covariance matrix* learning and *bimodal distribution* parameter setting, which improved the balance between local exploitation and global exploration abilities of DE. Cui et al. [13] introduced a novel ABC variant with depth-first search framework and *elite*-guided search equations, called DFSABC_elite, to achieve a better tradeoff between exploration and exploitation. RDPSO [14], a novel efficient PSO variant, was proposed based on the free electron model in metal conductors exposed to an external electric field. Later, an IRDPSO [14] was presented to further improve the performance of RDPSO. EPSO [15] introduced an ensemble of PSOs with self-adaptive mechanism. New algorithms like GWO [16] and WOA [17] are attracting significant attention too.

The GSA [18], inspired by the law of gravity and mass interactions, became very popular in a very short time, showing superior performance in solving various real-life complex optimization problems, such as [19], and is often adopted due to its several significant features [18].

1) A particle in GSA is guided by the sum of gravitational forces acting on it from all its neighbors stored in an elite archive K_{best}, rather than only one fittest particle in algorithms like canonical PSO model. This endows GSA with a unique attribute, i.e., diverse search directions.
2) The gravitational constant is reduced exponentially with time to judiciously balance the exploration and exploitation and speed up the convergence process. Also, the size of K_{best}, with the initial value $K_0 = P$ (P is the number of particles), decreases linearly over time and thus, exploration gradually disappears and exploitation begins to appear. By adjusting the size of K_{best}, the tradeoff between both phases can be approved for GSA.
3) Better particles have larger gravitational masses which cause higher intensities of attraction and, as a consequence, the particles tend to move toward the fittest particle. This permits a faster convergence. Conversely, particles with heavy inertial mass move at a slower pace and therefore search the problem space more locally and precisely, giving the flavor of an *adaptive learning rate*.
4) GSA is *memory-less*. However, it functions efficiently like the methods with memory. The seminal paper [18] demonstrates superior convergence rate of GSA over PSO and Real GA, two of the most popular MHS algorithms.

Various GSA variants, such as an improved GSA proposed in [20], adaptive gbest-guided GSA [21], etc., have shown improved performance vis-à-vis basic GSA. However, very few studies have addressed the problems caused by the K_{best} model [22]. Recently, proposed DNLGSA [22] incorporated the *local* and *global neighborhood topologies* to effectively balance the exploration and exploitation and enhance the performance of GSA. The K_{best} model is replaced in DNLGSA. Moreover, our experimental studies reveal that DNLGSA is significantly faster and more accurate than the GSA, when implemented for our real-life problem.

However, in the practical engineering applications of metaheuristics, obtaining acceptable solutions in a very short time always remains a point of focus. To find an acceptable or near-optimal solution fast and efficiently in a real-life problem, a MHS algorithm must possess a superior exploration capability. Population diversity is very crucial in MHS algorithms to enable efficient global exploration and to avoid abysmal performance because of premature convergence [22]. Now, population diversity in DNLGSA gets noticeably influenced

by the degrees of uniformity and correlation of the random numbers involved in the calculation of the particle velocities. If a random number generator which generates sequences of numbers showing superior statistical properties can be used, then the optimal performance of DNLGSA can be further improved. The present work introduces an advanced variant of DNLGSA called CEDNLGSA where the authors propose to utilize a new PRNG based on the state-time histories of a FOChS [24], to generate random numbers for calculating the particle velocities. Various statistical tests for distribution and independence also confirm the superiority of the proposed FOChS-PRNG over one of the most extensively used general purpose PRNG, namely MT-PRNG [23]. Fractional-order extensions of the integer-order chaotic systems demonstrate more abundant dynamic characteristics compared to the original integer order versions, due to their *nonlocal* features and significant *nonlinear* behavior [25], and the sequences of PRNs produced with them show further improved degrees of uniformity and independence.

In this work, we propose an inexpensive, yet appealing new sonar-based solution for human localization in human–robot coexisting environments that can be particularly effective for solving the bad initialization problem encountered by the traditional local optimizer-based sonar scan matching methods. Our main aim is to accurately estimate the motion of the leg-pair of a walking human between two successive sonar scans gathered by the onboard sonar arrangement of a mobile robot with respect to a specific RPF [26], during people tracking. For this purpose, we first utilize density-based clustering, followed by our proposed SCE method and recently developed EFBLR algorithm, to filter the scans by eliminating noises, discarding the readings indicating the static and nonhuman moving objects, and preserving the readings representing the target legs. Then we employ a novel variant of sNDT based on CEDNLGSA, called CMHS-sNDT, to determine the roto-translation of the target legs between the filtered scans, a robust solution that can specifically overcome bad initialization problems. This overall proposed approach for HLL is named here as HLL-CMHS-sNDT. This cycle of gathering two successive sonar scans at a certain RPF, removing outliers, static, and nonhuman moving objects and extracting target leg-pair from each sonar scan, and then accurately matching the two filtered scans using CMHS-sNDT to estimate the human motion between them, can be repeatedly implemented for subsequent pairs of scans, thus making the proposed approach suitable for following people in real-life.

The significant contributions of this research work are as follows.

1) In this work, a novel, robust approach is proposed to solve the bad initialization problem encountered in sonar scan matching, by embedding a MHS-based optimization mechanism in the sNDT method, a popular LF-based sonar scan matching technique. In this context, we develop a new MHS algorithm in the genre of GSA based on the state-time histories of a FOChS, named CEDNLGSA, which is aimed at improving the convergence performance and search ability of GSA, as well as maintaining a healthy population diversity.
2) We believe that this is the first study to demonstrate how a global search strategy can be effectively utilized to perform sonar scan matching and also the first research work to show how a global optimization-based sonar scan matching framework can be utilized to achieve accurate and robust human localization. Moreover, this is, to the best of our knowledge and belief, the first work to demonstrate a successful real-life implementation of a FOChS-based metaheuristic for solving sonar scan matching-based human localization problems.

Extensive experimentations and performance evaluations demonstrate superiority of the proposed method compared to the basic NWM-based sNDT and other popular metaheuristics-based variants of sNDT formulated in this work itself.

This article is organized as follows. Section II presents the basic framework of the HLL-CMHS-sNDT approach. Section III discusses the mechanism for the extraction of target leg points, using the SCE method in conjunction with the EFBLR algorithm. Sections IV and V describe CMHS-sNDT and CEDNLGSA, respectively. Real-life performances are evaluated in Section VI. Finally, the article is concluded in Section VII.

II. Basic Framework of HLL-CMHS-sNDT

In the HLL-CMHS-sNDT approach, for a specific robot pose, a couple of sonar scans are gathered corresponding to two distinct human leg poses at two successive time instants, and hence both scans are referred to two different RCFs[1] but a single and unique RPF[2] [7]. The first scan is called the *raw reference scan* and the second scan is called the *raw current scan*. Let a raw reference scan (denoted as $R\Upsilon_{\mathsf{rf}}$) be described by a set of B_s 2-D points $R\Upsilon_{\mathsf{rf}} = \{\mathbf{nr}_1, \ldots, \mathbf{nr}_{B_s}\}$ acquired at a RCF Cr at a sampling instant s with respect to a specific RPF α and a raw current scan (denoted as $R\Upsilon_{\mathsf{cr}}$) by a set of A_s 2-D points $R\Upsilon_{\mathsf{cr}} = \{\mathbf{mr}_1, \ldots, \mathbf{mr}_{A_s}\}$ at RCF Cc at the next sampling instant $s+1$ with respect to the same RPF α.

The goal of our HLL-CMHS-sNDT approach is to estimate the motion of the legs of a walking person between the RCFs $\mathsf{Cr} = \mathsf{rc}_s$ and $\mathsf{Cc} = \mathsf{rc}_{s+1}$, with respect to a particular RPF $\alpha = \mathsf{rp}_{[s,s+1]}$, by using an advanced scan matching technique [7]. Firstly, we employ DBSCAN, a density-based clustering method [27], separately on $R\Upsilon_{\mathsf{rf}}$ and $R\Upsilon_{\mathsf{cr}}$, to form arbitrarily shaped *significant* clusters of the data points characterizing static and moving objects, including the target person's legs and remove outliers. Then, the data points representing the moving objects are extracted using the SCE method, resulting in *refined* $R\Upsilon_{\mathsf{rf}}$ and *refined* $R\Upsilon_{\mathsf{cr}}$. Next, the EFBLR algorithm is used to identify the target leg patterns in the refined $R\Upsilon_{\mathsf{rf}}$ and refined $R\Upsilon_{\mathsf{cr}}$, and subsequently, extract the leg points from the corresponding scans. Accordingly, the refined $R\Upsilon_{\mathsf{rf}}$ and refined

[1]The RCF rc_t represents the coordinate frame that is located at the set of range measurements constituting a scan acquired at an instant of time t by the onboard ultrasonic sensing configuration.

[2]The RPF rp_t represents the coordinate frame that is located at the robot pose at an instant of time t [26].

$R\Upsilon_{\mathsf{cr}}$ are modified to *reference* and *current scans*, represented by $\Upsilon_{\mathsf{rf}} = \{\mathbf{n}_1, \ldots, \mathbf{n}_B\}$ and $\Upsilon_{\mathsf{cr}} = \{\mathbf{m}_1, \ldots, \mathbf{m}_A\}$, respectively.

Next, a novel scan matching algorithm based on the theory of LF is proposed, named here CMHS-sNDT algorithm, to determine the best estimate of the relative position of the target person's leg pair between the two LRFs [7] $\mathsf{Fr} = \mathsf{lr}_s$ and $\mathsf{Fc} = \mathsf{lr}_{s+1}$, with respect to the RPF α. In the context of scan matching here, we redefine the original RCF as the LRF [7]. In the CMHS-sNDT algorithm, we first build several overlapping sNDT grids having different positions of the origin from the set of target leg points belonging to Υ_{rf}. For each cell of a specific grid containing at least a certain number of points, a model which optimally fits the inliers (and discards the outliers) of the set of data points contained in the corresponding cell is discovered by making use of the RANSAC/GD method. Then, with the help of RANSAC/GF technique, we extract the points in Υ_{cr} which render the *generative process* assumption valid [8]. After constructing the overlapping sNDT grids and filtering Υ_{cr}, we perform the scan matching process by using our proposed CEDNLGSA. The corresponding scan matching estimate is indicated by ${}_{\mathsf{Fr}}\mathbf{z}^{(\alpha)}_{\mathsf{Fc}}$, represented as a multivariate Normal distribution ${}_{\mathsf{Fr}}\mathbf{z}^{(\alpha)}_{\mathsf{Fc}} = \mathcal{N}({}_{\mathsf{Fr}}\overline{\mathbf{z}}^{(\alpha)}_{\mathsf{Fc}}, {}_{\mathsf{Fr}}\mathbf{P}^{(\alpha)}_{\mathsf{Fc}})$, where ${}_{\mathsf{Fr}}\overline{\mathbf{z}}^{(\alpha)}_{\mathsf{Fc}}$ indicates the mean vector of the form $[d_x, d_y, \phi]^T$ (d_x and d_y symbolize the translations in the x- and y-directions, respectively, and ϕ stands for the rotation), and ${}_{\mathsf{Fr}}\mathbf{P}^{(\alpha)}_{\mathsf{Fc}}$ denotes the covariance matrix [7]. The scan matching problem here estimates the motion of the leg pair of a target person ${}_{\mathsf{Fr}}\mathbf{z}^{(\alpha)}_{\mathsf{Fc}}$ which maximizes the *overlap* between Υ_{rf} and Υ_{cr}.

The proposed HLL-CMHS-sNDT approach can be utilized in human–robot coexisting environments for estimating the trajectory of a walking person using scans within an angular span of 180° obtained from a sonar sensor mounted on a wheeled mobile robot. Our proposed HLL algorithm finds scan matching estimate between a pair of scans gathered at successive sampling instants, and this algorithm is repeatedly run for subsequent pairs of scans so that the mobile robot can follow a walking person in real-life. At first, a pair of scans is gathered for a specific robot pose at two consecutive sampling instants, which are used by the proposed CMHS-sNDT to estimate the motion of the target person's leg-pair between the two time instants. Next, the robot moves and another pair of scans is acquired at successive sampling instants and again the human motion between the corresponding time instants is estimated. This sequence of events is then performed in an iterative fashion. Inspired by our recent work in [7], the flowchart of the proposed HLL-CMHS-sNDT approach for HLL and following is presented in Fig. 1.

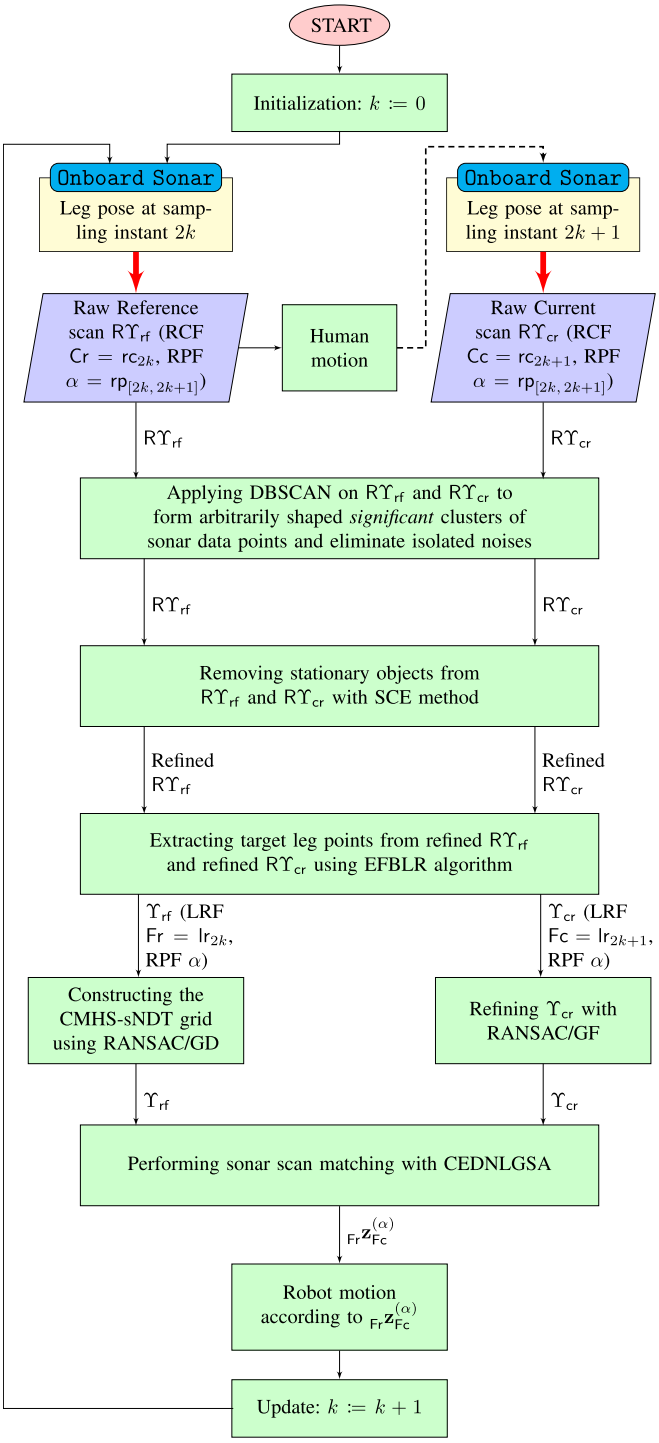

Fig. 1. Flowchart of the proposed HLL-CMHS-sNDT approach for HLL and following.

III. Target Leg Points Extraction

A. Moving Object Recognition With SCE Method

For each raw reference scan $R\Upsilon_{\mathsf{rf}}$ and raw current scan $R\Upsilon_{\mathsf{cr}}$, the DBSCAN algorithm first clusters sonar data points using the notions of *density-reachability* and *density-connectivity*, characterized by a *distance threshold* $\epsilon > 0$ and a *density threshold* MinPts [27]. Next, to extract the moving objects from both the *noise-free* scans and eliminate the remaining points (basically characterizing static obstacles), we propose a method called SCE method. Here, we compute the centroids of all the clusters associated with both the scans $R\Upsilon_{\mathsf{rf}}$ and $R\Upsilon_{\mathsf{cr}}$, and then evaluate the displacements of the cluster centroids belonging to $R\Upsilon_{\mathsf{rf}}$ from their original initial positions by using the locations of the cluster centroids belonging to $R\Upsilon_{\mathsf{cr}}$. This facilitates detection of the movement of the moving objects between $R\Upsilon_{\mathsf{rf}}$ and $R\Upsilon_{\mathsf{cr}}$ and identification of the points representing those objects in both

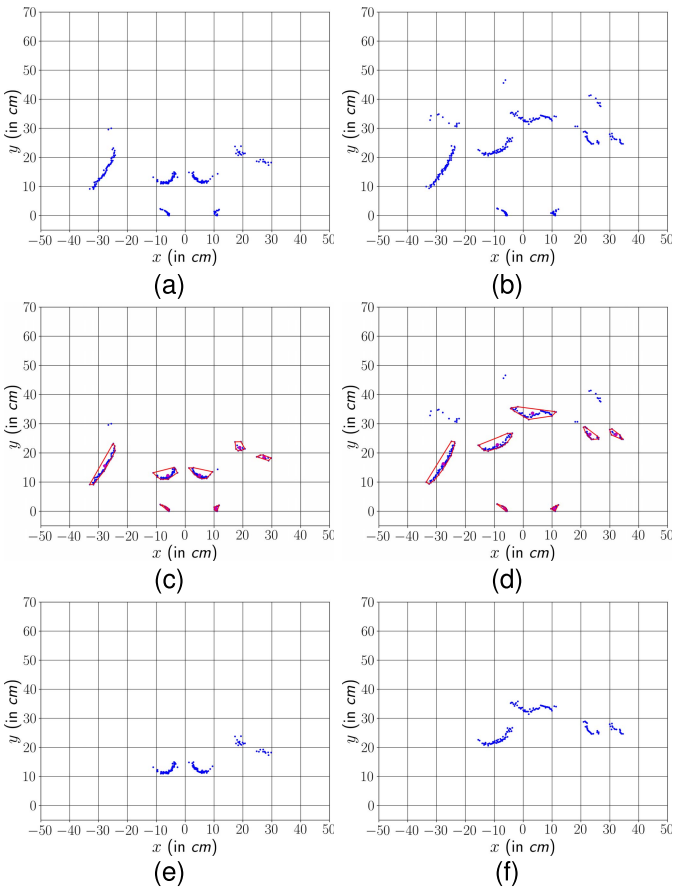

Fig. 2. (a) and (b) Data points in a representative $R\Upsilon_{\mathsf{rf}}$ and a representative $R\Upsilon_{\mathsf{cr}}$, respectively. (c) and (d) *Significant* clusters of the data points in $R\Upsilon_{\mathsf{rf}}$ and $R\Upsilon_{\mathsf{cr}}$, respectively, formed with DBSCAN and the corresponding cluster centroids. A *red* contour: a cluster and a *magenta* dot: its centroid. (e) and (f) Data points representing the moving objects, extracted from $R\Upsilon_{\mathsf{rf}}$ and $R\Upsilon_{\mathsf{cr}}$, respectively, using SCE method. Accordingly, $R\Upsilon_{\mathsf{rf}}$ and $R\Upsilon_{\mathsf{cr}}$ are transformed into the *refined* $R\Upsilon_{\mathsf{rf}}$ and *refined* $R\Upsilon_{\mathsf{cr}}$, respectively.

the scans. However, due to uncertainties involved in sonar sensing, a cluster centroid belonging to $R\Upsilon_{\mathsf{rf}}$ which has not actually moved with respect to its original initial position, may report spurious displacement in $R\Upsilon_{\mathsf{cr}}$. A *radius threshold* rd_{th} signifying a tolerance level has been introduced to overcome this problem.

Let $\mathbf{Cn_r} = \{\mathsf{Cn}_{\mathsf{r}_i}\}_{i=1}^{J}$ and $\mathbf{Cn_c} = \{\mathsf{Cn}_{\mathsf{c}_j}\}_{j=1}^{K}$ be the sets of cluster centroids associated with $R\Upsilon_{\mathsf{rf}}$ and $R\Upsilon_{\mathsf{cr}}$, respectively. For a $\mathsf{Cn}_{r_i} \in \mathbf{Cn_r}$ if there exists a $\mathsf{Cn}_{\mathsf{c}_j} \in \mathbf{Cn_c}$ such that

$$\left\| \mathsf{Cn}_{r_i} - \mathsf{Cn}_{\mathsf{c}_j} \right\| \leq rd_{\text{th}} \tag{1}$$

then the pair $\{\mathsf{Cn}_{r_i}, \mathsf{Cn}_{\mathsf{c}_j}\}$ is referred to as the *static centroid doublet* and both the centroids Cn_{r_i} and $\mathsf{Cn}_{\mathsf{c}_j}$ are queued into a list $\mathscr{C}_{\text{stat}}$. Once the tasks of detecting the static centroid doublets and inserting them into $\mathscr{C}_{\text{stat}}$ are completed, we populate the remaining centroids from both the scans into another list $\mathscr{C}_{\text{mov}}$ and designate the group of the centroids belonging to $\mathscr{C}_{\text{mov}}$ as the *moving centroid combination*. Next, the clusters corresponding to the centroids in $\mathscr{C}_{\text{stat}}$ are removed and the clusters corresponding to the centroids in $\mathscr{C}_{\text{mov}}$ (i.e., the moving objects) are preserved. The proposed SCE method, which outputs the *refined* $R\Upsilon_{\mathsf{rf}}$ and *refined* $R\Upsilon_{\mathsf{cr}}$, is illustrated with a representative real-life example in Fig. 2, where the walking target person, a walking cat, and several static obstacles are present in the scanned environment.

B. Target Leg-Pair Identification With EFBLR Algorithm

Then to recognize the moving target leg-pair, we employ our recently developed EFBLR algorithm [7] that detects the target person's legs in a sonar scan acquired during human following within a *leader-follower* framework. The algorithm, for specific leg poses, identifies typical leg patterns, which are readily distinguishable from other objects in a real-life human–robot coexisting environment. The refined $R\Upsilon_{\mathsf{rf}}$ and refined $R\Upsilon_{\mathsf{cr}}$ comprising the readings of the moving clusters (objects) are next input to the EFBLR algorithm. In this algorithm, a set of range measurements $\mathscr{A}_{\mathsf{rg}}$ is maintained as [7]

$$\mathscr{A}_{\mathsf{rg}} = \{\mathsf{rg}_1, \ldots, \mathsf{rg}_{\mathsf{FS}}\}, \text{ with } \mathsf{rg}_j = \begin{cases} \hat{\mathsf{r}}\big|_{\psi_j}, & \text{if } \hat{\mathsf{r}}\big|_{\psi_j} \neq \mathtt{NaN} \\ \mathcal{S}_{\max}, & \text{if } \hat{\mathsf{r}}\big|_{\psi_j} = \mathtt{NaN} \end{cases}$$

where the constant term FS denotes the maximum possible number of readings in a scan in our work and $\hat{\mathsf{r}}|_{\psi_j}$ represents the range measurement in the direction ψ_j. The maximum sonar range $\mathcal{S}_{\max}$, in this case, is set at 70 cm.

From the set $\mathscr{A}_{\mathsf{rg}}$ of range readings, the identification of different leg patterns can be performed efficiently by utilizing a method based on the geometric features of *vertical edges*. Details of the methodology for detecting and listing vertical edges are given in [7]. Given vertical edges are classified into two categories: *falling* and *rising* edges, we elicit a subset from the complete list of connected edges, which might correspond to one of the four possible leg patterns: TLA, SJM, FWS, and TLT. To best represent these human leg patterns, four ordered sequences comprising falling/rising edges are defined as: 1) TLA: a quadruplet $\{\mathscr{F}, \mathscr{R}, \mathscr{F}, \mathscr{R}\}$; 2) SJM: a quadruplet $\{\mathscr{F}, \mathscr{R}, \mathscr{F}, \mathscr{R}\}$; 3) FWS: a triplet $\{\mathscr{F}, \mathscr{F}, \mathscr{R}\}$ or $\{\mathscr{F}, \mathscr{R}, \mathscr{R}\}$; and 4) TLT: a doublet $\{\mathscr{F}, \mathscr{R}\}$, with $\mathscr{F}$ and $\mathscr{R}$ denoting a falling edge and a rising edge, respectively. It is worth mentioning that, considering the short valid measurement distance of the sonar sensor, we have introduced a new pattern into the original EFBLR framework, namely SJM, to capture the forward jump motion of the target person because, on occasion, he/she may be required to jump once or twice while walking. The SJM pattern is based on the consideration that when one leg is swinging within the vertical *field of view* of the onboard sonar arrangement, the other one is in a stance state. Fig. 3 shows the four typical leg patterns, where several dimensional constraints are specified for the measures wid, sin, stp(J/F), and tog, respectively, denoting the single leg-width, the spatial interval between two legs, the step length for SJM/FWS pattern, and the collective width of two legs. For the settings wid $\in$ [10, 20] cm, sin $\in$ [7, 17] cm, stp(J) $\in$ [10, 20] cm, stp(F) $\in$ (20, 40] cm, and tog $\in$ [10, 40] cm, the optimal results are obtained.

The EFBLR algorithm for identification of the target leg pattern corresponding to a single sonar scan is detailed in [7]. The subroutines for the detection of SJM and TLA patterns are similar, except that instead of considering the geometric

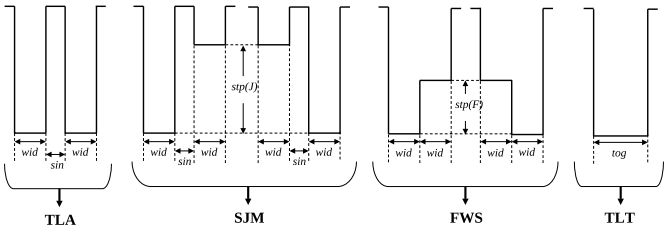

Fig. 3. Typical human leg patterns identified by the EFBLR algorithm.

constraints of the TLA pattern, one needs to adopt those of the SJM pattern. Now, once the leg pattern for a scan is recognized using the EFBLR algorithm, the corresponding sequences of $\mathscr{F}/\mathscr{R}$ edges and edge-indices [7] can be utilized to retrieve the set of data points representing the target leg-pair.

The EFBLR-based module for extracting the target leg points, which outputs the reference scan (denoted as Υ_{rf}) and current scan (denoted as Υ_{cr}), comprising B and A points, respectively, is illustrated in Fig. 4, where the module takes the refined $R\Upsilon_{\mathsf{rf}}$ and refined $R\Upsilon_{\mathsf{cr}}$ in Fig. 2 as its inputs.

IV. Development of the CMHS-sNDT

The proposed CMHS-sNDT method presents an accurate and robust LF-based solution to the sonar scan matching problems, where the original NDT [9] is suitably adapted to deal with the uncertainty and sparseness associated with sonar readings [8]. CMHS-sNDT introduces a grid-building mechanism [8], where each cell is modeled with a *Normal* distribution. Also, CMHS-sNDT introduces a scan-filtering procedure [8] and proposes a new chaotic metaheuristic optimization framework to perform scan matching.

A. Constructing the CMHS-sNDT Grid by Using RANSAC/GD

In CMHS-sNDT, the distribution of a sonar point cloud is modeled by a grid of *Normal* distributions constructed from $\mathbf{n}_{j=1,\ldots,B} \in \Upsilon_{\mathsf{rf}}$. The 2-D data space containing Υ_{rf} is divided into M square-shaped cells and the set of points $\mathbf{n}_j \in \Upsilon_{\mathsf{rf}}$ lying within each cell is then searched. Based on the position of the origin of the grid, the points belonging to Υ_{rf} are divided into different groups. Then, for a given cell k of a specific grid with origin σ consisting of no less than *three* points, we calculate the mean $\boldsymbol{\varrho}_{\sigma,k}$ and the covariance matrix $\mathbf{C}_{\sigma,k}$ of the set of points $\Psi_{\sigma,k}$ contained in that cell, required to obtain a bivariate *Normal* distribution $\mathcal{N}(\boldsymbol{\varrho}_{\sigma,k}, \mathbf{C}_{\sigma,k})$. For our sonar-based approach, where a significant number of *outliers* are usually present and due to these sensors' low angular resolution, dense regions of outliers (called *artifacts*) tend to be formed, we use RANSAC/GD [8] to estimate $\boldsymbol{\varrho}_{\sigma,k}$ and $\mathbf{C}_{\sigma,k}$ of $\mathcal{N}(\boldsymbol{\varrho}_{\sigma,k}, \mathbf{C}_{\sigma,k})$ that optimally fits the inliers of $\Psi_{\sigma,k}$.

B. Defining the LF Associated With the CMHS-sNDT Grid

Next, we model the probability of having a sonar reading at 2-D point $\mathbf{x}$ located inside the cell k by $\mathcal{N}(\boldsymbol{\varrho}_{\sigma,k}, \mathbf{C}_{\sigma,k})$. The

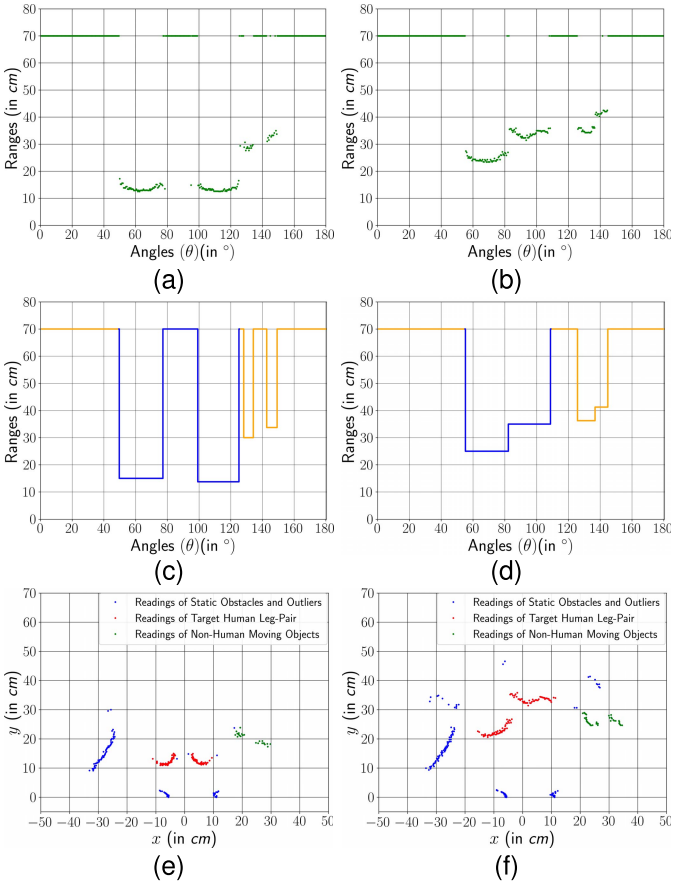

Fig. 4. (a) and (b) Cartesian graphs representing the remodeled range-arrays $\mathscr{A}_{\mathsf{rg}}$s corresponding to the refined $R\Upsilon_{\mathsf{rf}}$ [given in Fig. 2(e)] and refined $R\Upsilon_{\mathsf{cr}}$ [given in Fig. 2(f)], respectively (with range on the ordinate, and angle on the abscissa). (c) and (d) Target leg-pair patterns corresponding to the refined $R\Upsilon_{\mathsf{rf}}$ and refined $R\Upsilon_{\mathsf{cr}}$, respectively, identified by the EFBLR algorithm. The *blue* patterns indicate the pairs of the target person's legs. (e) and (f) Target leg points extracted from $R\Upsilon_{\mathsf{rf}}$ [given in Fig. 2(a)] and $R\Upsilon_{\mathsf{cr}}$ [given in Fig. 2(b)], respectively, based on the outputs of the EFBLR algorithm. Eventually, the refined $R\Upsilon_{\mathsf{rf}}$ and refined $R\Upsilon_{\mathsf{cr}}$ are modified to Υ_{rf} and Υ_{cr}, respectively, comprising the data points representing the moving target leg-pair.

LF corresponding to the cell k is defined as [8]

$$L_{\sigma,k}(\mathbf{x}) = \exp\left[-\frac{(\mathbf{x}-\boldsymbol{\varrho}_{\sigma,k})^T \mathbf{C}_{\sigma,k}^{-1}(\mathbf{x}-\boldsymbol{\varrho}_{\sigma,k})}{2}\right]. \tag{2}$$

Then the LF $L_\sigma(\mathbf{x})$ associated with the Υ_{rf} and the sNDT grid's origin σ can be given as [8]

$$L_\sigma(\mathbf{x}) = \begin{cases} L_{\sigma,1}(\mathbf{x}), & \mathbf{x} \in \Psi_{\sigma,1} \\ \quad\cdots & \\ L_{\sigma,M}(\mathbf{x}), & \mathbf{x} \in \Psi_{\sigma,M}. \end{cases} \tag{3}$$

Following the seminal NDT approach, we also use *four* overlapping grids [9], to compute the LF at position $\mathbf{x}$ [8]

$$L(\mathbf{x}) = \sum_{1\le\sigma\le 4} L_\sigma(\mathbf{x}). \tag{4}$$

Fig. 5 depicts the results of constructing the CMHS-sNDT grid using the RANSAC/GD algorithm with various values of *narrowness factor* [8]. In fact, the LF gets narrower as the narrowness factor decreases and a narrow LF may be problematic if bad initialization data is provided.

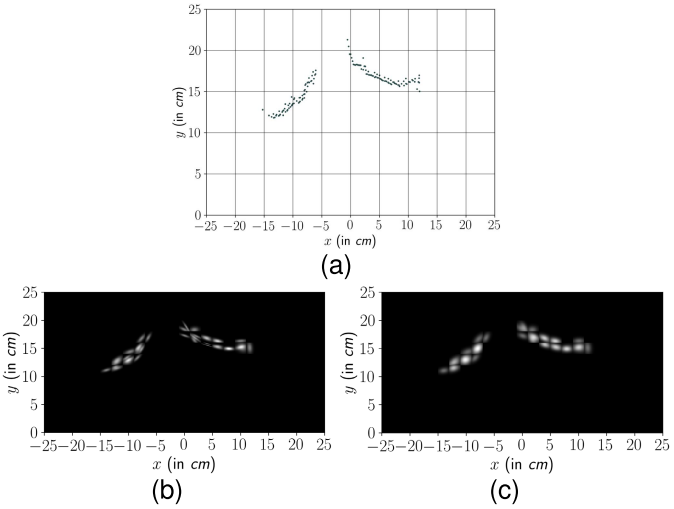

Fig. 5. (a) Sample sonar scan containing noisy and spurious leg point data. The results of building the CMHS-sNDT grid from the scan in Fig. 5(a) by using the RANSAC/GD with various narrowness factors: four overlapping grids with narrowness factor set to (b) 0.001 (usually used for laser counterpart) and (c) 0.5.

C. Filtering Sonar Scans

In the CMHS-sNDT approach, Υ_{rf} is used to construct the LF, whereas Υ_{cr} is used as a *point cloud*. Hence, it is crucial for Υ_{cr} to posses the similar characteristics as Υ_{rf}. Now, the inliers chosen from Υ_{rf} by the RANSAC/GD algorithm are used to construct the CMHS-sNDT grid. A similar approach, referred to as RANSAC/GF [8] is employed for Υ_{cr} which filters the sonar readings in Υ_{cr} such that the *generative process* assumption [8] holds valid. Hence Υ_{cr} gets split into two subsets: 1) the *adopted readings* comprise data fulfilling the generative process assumption and 2) the *rejected readings* comprising the rest data [8].

D. Performing Sonar Scan Matching

Next, CMHS-sNDT computes the *scan matching estimate* by minimizing a score function $\mathsf{SF}(\mathbf{z})$ with the CEDNLGSA. The score function $\mathsf{SF}(\mathbf{z})$ is defined according to [8] as

$$\mathsf{SF}(\mathbf{z}) = -\sum_{\mathbf{m}_i \in \Upsilon_{\mathsf{cr}}} \sum_{1 \le \sigma \le 4} L_\sigma(\mathbf{z} \oplus \mathbf{m}_i) \tag{5}$$

where $\mathbf{z} = [d_x,\, d_y,\, \phi]^T$ indicates a roto-translation between the LF and the Υ_{cr} LRF, and the operator $\oplus$ indicates composition of transformations. The score function $\mathsf{SF}(\mathbf{z})$ evaluates the goodness of the roto-translation $\mathbf{z} = [d_x,\, d_y,\, \phi]^T$ between Υ_{rf} and Υ_{cr} and when it achieves its minimum value, the CMHS-sNDT designates the corresponding roto-translation as the scan matching estimate ${}_{\mathsf{Fr}}\mathbf{z}_{\mathsf{Fc}}^{(\alpha)}$. In our proposed CEDNLGSA, we represent a roto-translation with the position of a particle. Fig. 6 demonstrates the CMHS-sNDT approach with a representative real-life case study.

Because of space limitations, real-life case studies showing the successful implementation of our proposed methodologies for human leg points extraction and human leg motion estimation are presented in Section S-I of the "Supplementary File."

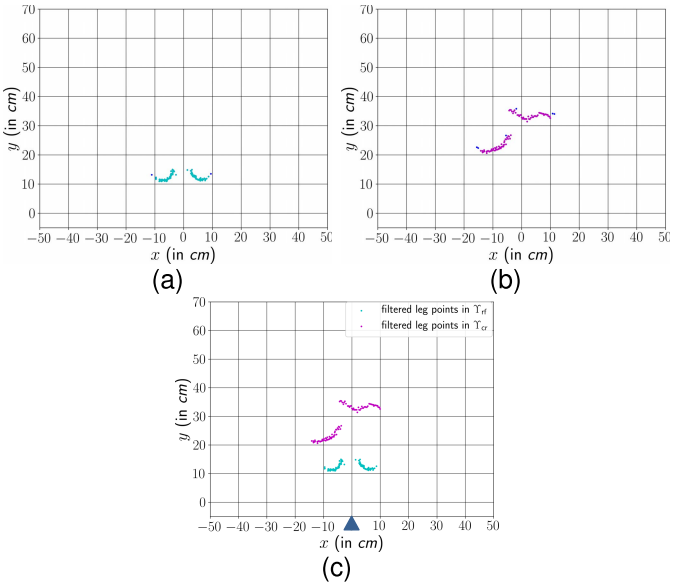

Fig. 6. (a) Set of readings in Υ_{rf} [given in Fig. 4(e)] selected as inliers by RANSAC/GD (output: *cyan* leg points). (b) Filtering Υ_{cr} [given in Fig. 4(f)] with RANSAC/GF (output: *magenta* leg points). (c) *Filtered* sets of leg points in Υ_{rf} and Υ_{cr} with respect to a specific RPF α, on which CMHS-sNDT is implemented. The *blue* triangle represents the robot's position. The resulting scan-matching estimate: ${}_{\mathsf{Fr}}\mathbf{z}_{\mathsf{Fc}}^{(\alpha)} = [-2.87\text{ cm},\ 15.21\text{ cm},\ 0.59\text{ rad}]^T$.

V. Proposed CEDNLGSA

A. Chaos-Based PRN Generation for the Proposed CMHS Algorithm

In order to generate sequences of PRNs for CEDNLGSA, we propose to use the state-time histories of a popular FOChS, namely FOVlS, which are calculated by making use of the well-established G-L definition [24] of fractional calculus. This is the first work, according to the best of our knowledge and belief, to demonstrate a successful real-life implementation of these concepts for sonar scan matching-based human localization problems.

1) Fractional Order Volta's System: The state-time histories of FOVlS have been utilized to develop our proposed chaos-based PRNG. The fractional order version of Volta's system is given as [24]

$$\begin{aligned}
{}_0\mathscr{D}_t^{\beta_1} y_1(t) &= \Phi_1(y_1(t), y_2(t), y_3(t), t) \\
&= -y_1(t) - a y_2(t) - y_3(t) y_2(t) \\
{}_0\mathscr{D}_t^{\beta_2} y_2(t) &= \Phi_2(y_1(t), y_2(t), y_3(t), t) \\
&= -y_2(t) - b y_1(t) - y_1(t) y_3(t) \\
{}_0\mathscr{D}_t^{\beta_3} y_3(t) &= \Phi_3(y_1(t), y_2(t), y_3(t), t) \\
&= c y_3(t) + y_1(t) y_2(t) + 1
\end{aligned} \tag{6}$$

where $0 < \beta_1,\, \beta_2,\, \beta_3 \le 2$ are the fractional derivative orders and $(a,\, b,\, c) \in \mathbb{R}^3$ are system parameters.

The numerical solution of the FOVlS (6) based on the G-L definition can be given by the following expression,

as described in [24]:

$$y_i(t_j) = \Phi_i\big(y_1(t_{j-1}), y_2(t_{j-1}), y_3(t_{j-1}), t_{j-1}\big)h^{\beta_i} - \sum_{k=1}^{j} \mathscr{X}_k^{(\beta_i)} y_i(t_{j-k}) \tag{7}$$

where $i = 1, 2, 3$; $j = 1, 2, \ldots, W$, for $W = \lfloor T_s/h \rfloor$, T_s is the simulation time and h is a significantly small step size; $[y_1(t_0), y_2(t_0), y_3(t_0)]$ are the initial conditions. The binomial coefficients $\mathscr{X}_k^{(\beta_i)}, \forall i$, are computed as follows [24]:

$$\mathscr{X}_0^{(\beta_i)} = 1, \quad \mathscr{X}_k^{(\beta_i)} = \left(1 - \frac{1+\beta_i}{k}\right)\mathscr{X}_{k-1}^{(\beta_i)}. \tag{8}$$

A significant number of different combinations of (a, b, c) and $(\beta_1, \beta_2, \beta_3)$ can be chosen experimentally, for which the *necessary stability condition* for the *general incommensurate fractional order nonlinear system* to exhibit chaotic behavior [24] is satisfied by FOVIS (6). For example, when we consider the system parameters $a = 5$, $b = 85$, $c = 0.5$ and the fractional derivative (incommensurate) orders $\beta_1 = 0.89$, $\beta_2 = 1.10$, $\beta_3 = 0.91$ [24], FOVIS satisfies the necessary stability condition to remain chaotic.

2) Proposed Chaotic PRNG: We now propose a new FOChS-PRNG, which employs the time histories of the state variables y_1, y_2 and y_3 of FOVIS to generate *three* distinct sequences of PRNs, denoted as $\mathbf{Y}_1$, $\mathbf{Y}_2$ and $\mathbf{Y}_3$, by using the following equation:

$$\mathrm{Y}_i(t_j) = \{(|y_i(t_j)| \times 10^{\eta}) - (\lfloor |y_i(t_j)| \times 10^{\eta} \rfloor)\} \quad \text{for } i = 1, 2, 3; \quad j = 0, 1, \ldots, \lfloor T_s/h \rfloor; \quad \eta \in \{1, 2, 3\} \tag{9}$$

where, $\mathrm{Y}_i(t_j)$ indicates the PRNs generated with the 64-bit floating point values of $y_i(t_j)$. The PRNs belonging to an array $\mathbf{Y}_i$, $i \in \{1, 2, 3\}$ lie in the interval $[0, 1]$, and are uniformly distributed throughout the interval with virtually *zero* correlation. We can arbitrarily select the initial conditions for the purpose of generating the pseudorandom sequences.

The results in Table I demonstrate without vagueness that our FOChS-PRNG, for three benchmark statistical tests of distribution and independence, namely Chi-square test (χ^2), K-S test and SRCC test [4], is consistently superior to MT-PRNG, which encouraged us to formulate CEDNLGSA, a novel chaos-based variant of DNLGSA, for the purpose of solving our scan matching problem.

TABLE I

COMPARISON OF THE MEAN RESULTS OF VARIOUS STATISTICAL TESTS BETWEEN FOCHS-PRNG AND MT-PRNG. THE CRITICAL VALUES $\chi^2_{\kappa(\mathcal{C})}$, $\Delta_{(\mathcal{C})}$, AND $\mathcal{Z}_{s(\mathcal{C})}$ ARE CONSIDERED AT A LEVEL OF SIGNIFICANCE $\xi = 0.05$ [4]. WE FAIL TO REJECT THE NULL HYPOTHESIS $\mathcal{H}_0$ [4] IF $\chi^2_{\kappa} < \chi^2_{\kappa(\mathcal{C})}$, $\Delta < \Delta_{(\mathcal{C})}$, AND $-\mathcal{Z}_{s(\mathcal{C})} < \mathcal{Z}_s < \mathcal{Z}_{s(\mathcal{C})}$, WHERE $\chi^2_{\kappa(\mathcal{C})} = 233.99$, $\Delta_{(\mathcal{C})} = \frac{1.36}{\sqrt{\mathcal{L}}} = 0.03512$, AND $\mathcal{Z}_{s(\mathcal{C})} = 1.96$ [4]. HERE, $\kappa = 200$ AND $\mathcal{L} = 1500$ [4]

PRNG	Chi-Square Test [4]		K-S Test [4]	SRCC Test [4]	
	χ^2_{κ} [4]	p-value [4]	Δ [4]	ρ [4]	$\mathcal{Z}_s$ [4]
MT-PRNG	209.16	0.3793	0.0317	0.0425	1.1289
FOChS-PRNG	**185.48**	**0.7618**	**0.0121**	**0.0059**	**0.1566**

B. Dynamic Neighborhood Learning Scheme

Let $\boldsymbol{Z} = [\mathbf{z}_1, \ldots, \mathbf{z}_P]$ represents the positions of P particles constituting a GSA population, where $\mathbf{z}_k = [z_k^1, \ldots, z_k^{\mathfrak{d}}]$, $k = 1, \ldots, P$ indicates the position of the kth particle moving through a $\mathfrak{d}$-dimensional search space with the velocity $\boldsymbol{\vartheta}_k = [\vartheta_k^1, \ldots, \vartheta_k^{\mathfrak{d}}]$. Also, let the velocities of $\mathbf{z}_k$ at iterations τ and $\tau+1$ in the δth dimension be denoted by $\vartheta_k^{\delta}(\tau)$ (referred to as *current velocity*) and $\vartheta_k^{\delta}(\tau+1)$ (referred to as *next velocity*), respectively. In the dynamic neighborhood learning strategy, the entire population is first randomly divided into Q *non-overlapping* local neighborhoods, $\mathcal{LN} = \{\mathcal{LN}_1, \ldots, \mathcal{LN}_Q\}$, each comprising $S = P/Q$ number of particles [22] (here, we have set $P = 50$ and $Q = 5$).

The particle k in the local neighborhood $\mathcal{LN}_i$ at iteration τ [denoted as $\mathcal{LN}_i(\tau)$] experiences gravitational forces from the remaining particles of $\mathcal{LN}_i(\tau)$, and its next *local* velocity is computed as [22]

$$\mathscr{L}\vartheta_k^{\delta}(\tau+1) = \sum_{\substack{\mathbf{z}_l \in \mathcal{LN}_i(\tau) \\ \mathbf{z}_l \neq \mathbf{z}_k}} \mathrm{Y}_1 \cdot \mathscr{G}(\tau)\frac{\mathscr{M}_l(\tau)}{\mathscr{D}_{kl}(\tau) + \varrho}\big(z_l^{\delta}(\tau) - z_k^{\delta}(\tau)\big) \tag{10}$$

where $\mathrm{Y}_1 \in [0, 1]$ is a uniform PRN. $\mathscr{G}(\tau)$, the gravitational constant, is calculated as [18]

$$\mathscr{G}(\tau) = \mathscr{G}_0 \cdot \exp\left(-\gamma \cdot \frac{\tau}{\mathrm{T}_{\mathsf{MAX}}}\right) \tag{11}$$

where $\mathscr{G}_0$ represents the initial value of the gravitational constant, γ is the attenuation coefficient, and $\mathrm{T}_{\mathsf{MAX}}$ is the maximum number of iterations cycles.

$\mathscr{M}_l(\tau)$, the mass of particle l at iteration τ is [18]

$$\mathscr{M}_l(\tau) = \frac{\mu_l(\tau)}{\sum_{p=1}^{P}\mu_p(\tau)} \tag{12}$$

for

$$\mu_l(\tau) = \frac{\mathfrak{fit}_l(\tau) - \mathfrak{worst}(\tau)}{\mathfrak{best}(\tau) - \mathfrak{worst}(\tau)} \tag{13}$$

where $\mathfrak{fit}_l(\tau)$ is the fitness value of particle l at iteration τ. For a minimization problem [18]

$$\mathfrak{best}(\tau) = \min_{p\in\{1,2,\ldots,P\}} \mathfrak{fit}_p(\tau) \tag{14}$$

$$\mathfrak{worst}(\tau) = \max_{p\in\{1,2,\ldots,P\}} \mathfrak{fit}_p(\tau). \tag{15}$$

Also, the scalar $\mathscr{D}_{kl}(\tau)$ indicates the Euclidean distance between two particles k and l at iteration τ and is represented by: $\mathscr{D}_{kl}(\tau) = \|\mathbf{z}_k(\tau), \mathbf{z}_l(\tau)\|_2$; ϱ is a small positive constant; $z_k^{\delta}(\tau)$ and $z_l^{\delta}(\tau)$ indicate the positions of the particles k and l at time τ in the δth direction, respectively.

The particle k also gets guidance from the historically best experience of the entire population, denoted by $\mathbf{gb} = [\mathsf{gb}^1, \mathsf{gb}^2, \ldots, \mathsf{gb}^{\mathfrak{d}}]$. Apparently, the $\mathbf{gb}$ model is analogous to a *global neighborhood* topology. For the particle k, its next *global* velocity, is defined as [22]

$$\mathscr{G}\vartheta_k^{\delta}(\tau+1) = \mathrm{Y}_2 \cdot \big(\mathsf{gb}^{\delta}(\tau) - z_k^{\delta}(\tau)\big) \tag{16}$$

where $\mathrm{Y}_2 \in [0, 1]$ is a uniform PRN.

The next resultant velocity of the particle k is computed as [22]

$$\vartheta_k^{\delta}(\tau+1) = \mathsf{Y}_3 \cdot \vartheta_k^{\delta}(\tau) + a_1 \cdot \mathscr{L}\vartheta_k^{\delta}(\tau+1) + a_2 \cdot \mathscr{G}\vartheta_k^{\delta}(\tau+1) \quad (17)$$

where $\mathrm{Y}_3 \in [0,\ 1]$ is a uniform PRN, and two acceleration coefficients, a_1 and a_2, are arbitrary non-negative numbers. If $a_1 > a_2$, *exploration* dominates, while if $a_2 > a_1$, *exploitation* dominates. Inspired by the adaptive adjustment in [22], we set $a_1 = 0.5 - 0.5\tau^{1/6}/\mathrm{T}_{\mathsf{MAX}}^{1/6}$ and $a_2 = 1.5\tau^{1/6}/\mathrm{T}_{\mathsf{MAX}}^{1/6}$. The position of particle k in the δth dimension is updated as [22]

$$z_k^{\delta}(\tau+1) = z_k^{\delta}(\tau) + \vartheta_k^{\delta}(\tau+1). \quad (18)$$

Here, Y_1, Y_2 and Y_3 are uniform PRNs corresponding to a value of the states y_1, y_2 and y_3 of the FOVlS, respectively.

The local neighborhood topology drastically reduces the computational complexity while maintaining the search diversity of GSA. Also, the global neighborhood topology is beneficial to accelerate the rate of convergence. Therefore, by proficiently combining both topologies, CEDNLGSA strengthens the balance between exploration and exploitation.

C. Framework of Dynamic Local Neighborhood Formation and **gb** Mutation

1) Convergence Criteria: The problem of particles getting trapped in local optima is addressed by using a dynamic local neighborhood formation strategy and a **gb** mutation mechanism based on two convergence criteria: the *limiting threshold* and the *population diversity* [22].

If the **gb** cannot better the self-solution after a definite number of successive iterations (c_{ind}), it may cause population stagnation and premature convergence. A limiting threshold C_{TH} is introduced to check the possibility of falling into stagnation. Once the risks of stagnation are identified, dynamic reformulation of the local neighborhoods and mutation of the **gb** are carried out to overcome it, based on the population diversity indicator. For computing population diversity at iteration τ [denoted as $\mathsf{PDV}(\tau)$], we first calculate the geographical clustering centroid of each local neighborhood at iteration τ

$$\mathcal{CLN}_j(\tau) = \frac{\sum_{\mathbf{z}_i \in \mathcal{LN}_j(\tau)} \mathbf{z}_i}{S}. \quad (19)$$

Then the distribution diversity of the centroids is given as [22]

$$\mathsf{PDV}(\tau) = \frac{1}{Q}\sum_{j=1}^{Q}\sqrt{\sum_{\delta=1}^{\mathfrak{d}}\left(\mathcal{CLN}_j^{\delta}(\tau) - \overline{\mathcal{CLN}^{\delta}}(\tau)\right)^2} \quad (20)$$

where

$$\overline{\mathcal{CLN}^{\delta}}(\tau) = \frac{\sum_{j=1}^{Q}\mathcal{CLN}_j^{\delta}(\tau)}{Q}. \quad (21)$$

2) Dynamic Reorganization of Local Neighborhoods and Mutation of **gb***:* If $c_{\mathrm{ind}} > C_{\mathrm{TH}}$, we compute population diversity and compare it with a *threshold of population diversity* ν which is employed to distinguish between exploration and exploitation [22]. Based on the result, Evolutionary State 1 or 2 is executed.

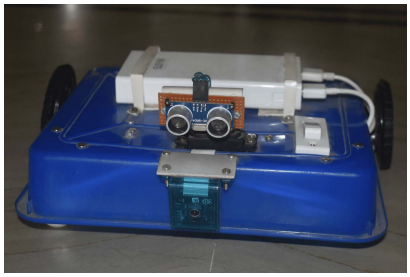

Fig. 7. Wheeled mobile robot employed for testing and implementing the proposed HLL-CMHS-sNDT method.

EVOLUTIONARY STATE 1 ($\mathsf{PDV} > \nu$): Here, the particles need to concentrate more on exploration in order to prevent the potential hazards of population stagnation. So, we carry out reformulation of the local neighborhoods and introduce the mutation of **gb** with large jump steps, given as [22]

$$\mathsf{nextgb}^{\delta}(\tau) = \mathsf{gb}^{\delta}(\tau) + \mathsf{PDV} \cdot \mathscr{UN}, \quad \text{if} \quad \mathsf{PDV} > \nu \quad (22)$$

where $\mathscr{UN}$ is a uniform PRN with range $[-1, 1]$, ensuring mutation in diverse directions.

EVOLUTIONARY STATE 2 ($\mathsf{PDV} \leq \nu$): Here CEDNLGSA should concentrate on exploitation. We introduce a mutation scale $\varphi \in (0,\ 1)$ to adjust the step size of the population diversity-based mutation mechanism as follows [22]:

$$\mathsf{nextgb}^{\delta}(\tau) = \mathsf{gb}^{\delta}(\tau) + \varphi \cdot \mathsf{PDV} \cdot \mathscr{UN}, \quad \text{if} \quad \mathsf{PDV} \leq \nu. \quad (23)$$

Furthermore, with the aim of promoting the evolution of our MHS algorithm to the global optimum, we adopt the next global best particle (**nextgb**) if it is better than the preceding one, otherwise we preserve the previous **gb**.

VI. Experimental Results and Performance Evaluations

A. Experimental Setup

Keeping the requirements in developing countries in mind, a low-cost, lightweight system has been implemented on an indigenously developed DD-WMR, shown in Fig. 7. The onboard computer is a Raspberry Pi 3 (in short: RPi) model B+ containing a 1.4 GHz 64-bit quad-core ARM Cortex-A53 processor along with 1 GB of LPDDR2 SDRAM [28]. The robot is equipped with an RPi Camera Module v2 comprising a Sony IMX219 8-Mpixel sensor [29] and an HC-SR04 ultrasonic sensor [30] for acquiring real-world visual and range data, respectively. Our DD-WMR is driven by only two motors, with a third servo motor rotating the ultrasonic sensor to collect sonar readings within a 180° wide angular range.

Our DD-WMR is built with ultrasonic and vision sensors with an aim of developing a human detection and tracking framework in which the sensors will work in both independent and cooperative manners so that the robot can either use a single sensor or a combination of both [5]. With such a provision, the system becomes potentially robust to the failure of any one sensing unit. In this research work, the ultrasonic ranging module HC-SR04 has been independently

used to perform localization of a person walking in front of our DD-WMR. The economical HC-SR04 ultrasonic sensor [30] whose weight is 10 g (approximately), reads, in practice, from 2 to 80 cm within a 30° cone, and is accurate to the nearest 0.3 cm. The operating voltage and working current of the sensor are +5 V dc and 15 mA (max), respectively (hence can be directly powered via the RPi's 5 V output). For the purpose of real-life implementation, the whole software has been written in `Python` in combination with `Cython`. Performance evaluations are carried out with the `NumPy` and `SciPy` libraries in Python, whereas the experimental results are plotted with the Python library `Matplotlib`.

Our HLL-CMHS-sNDT approach is quantitatively compared with the HLL approach using the original NWM-based sNDT (referred to as HLL-sNDT) and the human localization approaches using six popular contemporary MHS algorithms, namely DNLGSA [22], GWO [16], CoBiDE [12], DFSABC_elite [13], IRDPSO [14], and EPSO [15] based variants of sNDT formulated by us in the context of this article (referred to as HLL-Y-sNDT where Y is DNLGSA, GWO, CoBiDE, DFSABC_elite, IRDPSO, and EPSO, respectively). The values of the parameters used for the competing MHS algorithms are the same as those reported in the corresponding seminal papers. The experiments discussed in this section are performed using real-world sonar data sets gathered in *four* diverse real-life environments: 1) a corridor with multiple door frames and smooth concrete walls; 2) an unstructured room incorporating tables, chairs, and cardboard boxes; 3) an enclosed space comprising a combination of concrete walls, concrete structures, wooden walls and wooden doors; and 4) an enclosed space containing stone walls, glass doors, and steel furniture. The acquired data sets thus involve structured and unstructured regions, posing various challenging difficulties to our sonar sensing system. In each environment, two raw sonar scans $R\Upsilon_1$ and $R\Upsilon_2$ are acquired for a specific leg posture at two successive sampling instants t and $t+1$, respectively, with respect to a certain RPF α_0, and a third scan $R\Upsilon_3$ is acquired for a different leg posture at the subsequent sampling instant $t+2$ with respect to the same RPF α_0. Then, the scans $R\Upsilon_1$ and $R\Upsilon_2$, based on the SCE method and EFBLR algorithm, were transformed to Υ_1 and Υ_2, respectively, with the help of $R\Upsilon_3$. Moreover, the set of readings in Υ_1 selected as inliers by RANSAC/GD is adopted and Υ_2 is filtered with RANSAC/GF. Clearly, the roto-translation between Υ_1 and Υ_2 is perfectly known to be $[0\,\text{cm}, 0\,\text{cm}, 0\,\text{rad}]^T$ [8]. That is to say, the *ground truth* is available. Note that, although the scans $R\Upsilon_1$ and $R\Upsilon_2$ are gathered in similar real situations, Υ_1 and Υ_2 are not necessarily identical, thus setting up a realistic test bench for the sonar scan matching methods [8]. Furthermore, by considering two scans acquired for the same human pose with respect to a specific RPF, the experiments essentially focus on the matching capabilities of the methods.

A group of five experiments has been carried out in each environment, incorporating various initial location errors. The error values are randomly chosen according to uniform distributions ranging from -0.05 to 0.05 m in d_x and d_y, and from $-9°$ to 9° in ϕ in Experiment 1. The initial location error rises as we gradually move toward Experiment 5, where

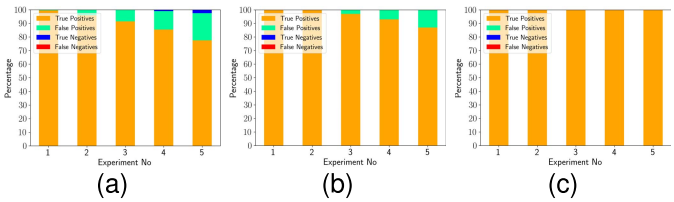

Fig. 8. Robustness of the competing HLL approaches: (a) HLL-sNDT, (b) HLL-CoBiDE-sNDT, and (c) HLL-Z-sNDT (Z: CMHS, EPSO, GWO, IRDPSO, DFSABC_elite, and DNLGSA).

the random errors lie between -0.25 and 0.25 m in d_x and d_y, and between $-45°$ and 45° in ϕ. These introduced errors correspond to the values assigned to the initial scan-matching estimate in Newton's algorithm. On the other hand, in the case of a single run of an MHS algorithm, randomly initializing the positions of P number of particles in a specific search space of d_x, d_y and ϕ can be viewed as analogous to introducing initial location errors lying within the same search space. To alleviate stochastic errors, the procedure is repeated 50 times for each experiment and scan, thus constituting $5 \times 4 \times 50 = 1000$ trials per algorithm and a total of $8 \times 1000 = 8000$ runs.

B. Scan Matching Performance Comparisons

We first compare, in statistical terms, the performances of the competing optimization algorithms in optimizing the score function $\mathsf{SF}(\mathbf{z})$ (5) (for details, see Section S-II of the "Supplementary File"). Next, we evaluate and compare the scan-matching performances of the HLL approaches based on those optimizers, in terms of *robustness*, *accuracy*, *speed of convergence*, and *computation time* [8]. Here, the term convergence refers to the ability of a method to satisfy numerical convergence criteria in a certain limited number of FEs. Considering real-life implementation, the computational budget for all the HLL methods has been limited to 1000 FEs.

1) Robustness: The robustness results for the competing HLL approaches are reported in Fig. 8. A trial is considered successful and a correct estimate is obtained if the absolute error is less than 0.075 m in d_x, 0.075 m in d_y and 0.075 rad in ϕ, and these threshold values are used to differentiate among *true positives*, *true negatives*, *false positives*, and *false negatives* [26]. Fig. 8 shows that the MHS-based HLL methods outperform HLL-sNDT and achieve superior robustness in the face of variations in initial error in different experiments conducted. As we can see, all the MHS-based HLL methods except HLL-CoBiDE-sNDT achieve 100% of true positives even in the most challenging situation of Experiment 5.

2) Accuracy: For measuring accuracy, we have considered the MAE of the positive estimates with respect to the ground truth roto-translation. By concentrating on the positive estimates, the experiment can assess the accuracy in real-life scenarios where ground truth may not be available and the method only can differentiate between positives and negatives. For this test, we have selected the angular error over the translational errors because the accurate computation of the former is considered a more critical component in the context of localization. As can be seen from Table II, HLL-CMHS-sNDT

TABLE II

COMPARISONS OF THE AVERAGE SCAN MATCHING PERFORMANCES OF THE COMPETING HLL APPROACHES

Human Leg Localization Approaches	EXPERIMENT 1			EXPERIMENT 2			EXPERIMENT 3			EXPERIMENT 4			EXPERIMENT 5		
	Accuracy MAE (in rad)	Speed of Convergence (FEs)	Computation Time (in s)	Accuracy MAE (in rad)	Speed of Convergence (FEs)	Computation Time (in s)	Accuracy MAE (in rad)	Speed of Convergence (FEs)	Computation Time (in s)	Accuracy MAE (in rad)	Speed of Convergence (FEs)	Computation Time (in s)	Accuracy MAE (in rad)	Speed of Convergence (FEs)	Computation Time (in s)
HLL-sNDT	2.31E-2	**016**	**0.671**	3.28E-2	**021**	**0.674**	4.61E-2	**025**	**0.676**	6.02E-2	**029**	**0.678**	7.64E-2	**032**	**0.679**
HLL-DNLGSA -sNDT	3.17E-8	050	0.685	4.78E-8	100	0.705	7.42E-8	150	0.726	1.19E-7	200	0.747	1.95E-7	250	0.769
HLL-GWO -sNDT	4.62E-8	060	0.708	1.31E-7	090	0.731	2.70E-7	150	0.776	4.82E-7	210	0.820	7.86E-7	300	0.888
HLL-CoBiDE -sNDT	1.14E-2	120	0.771	2.01E-2	180	0.825	3.26E-2	300	0.933	4.68E-2	420	1.041	6.37E-2	540	1.149
HLL-DFSABC_elite -sNDT	4.54E-6	050	0.719	8.27E-6	150	0.787	1.69E-5	150	0.861	2.86E-5	250	0.943	4.63E-5	350	1.055
HLL-IRDPSO -sNDT	8.41E-7	040	0.691	1.02E-6	080	0.719	1.45E-6	140	0.761	2.33E-6	200	0.803	4.24E-6	280	0.859
HLL-EPSO -sNDT	7.76E-4	047	0.692	1.25E-3	102	0.725	2.05E-3	176	0.769	3.50E-3	273	0.827	5.99E-3	397	0.901
HLL-CMHS -sNDT	**1.11E-8**	050	0.688	**1.67E-8**	100	0.704	**2.59E-8**	100	0.721	**4.10E-8**	150	0.740	**6.43E-8**	200	0.764

consistently achieves the best MAE performance between the rotations in the positive estimates and the ground truth rotation for all the experiments conducted.

3) Speed of Convergence and Computation Time: Here, the speed of convergence of a scan matching method is defined as the number of FEs until convergence in the case of true positive estimates. Table II summarizes the convergence speed and computation time results for the eight competing HLL approaches. It can be seen that, overall, our HLL-CMHS-sNDT only came second best in terms of both the convergence rate (in terms of FEs) and the computation times, where HLL-sNDT, a non-population-based algorithm, came first in both cases. However, in terms of robustness and accuracy, HLL-sNDT produced the worst result, as evident from Table II. Note that, in terms of convergence speed, some MHS-based HLL methods show better or comparable performances than CEDNLGSA-based approach when the initial error is low, primarily because of the variation in their population sizes. However, HLL-CMHS-sNDT outperforms those methods as the error increases. Similarly, although HLL-CMHS-sNDT requires fewer number of FEs than HLL-DNLGSA-sNDT as the initial error goes up, its computational time does not improve too much than HLL-DNLGSA-sNDT due to the involvement of chaos-based computations. However, HLL-CMHS-sNDT outperforms HLL-DNLGSA-sNDT in terms of accuracy in all the experiments, owing to the fact that the former one with its better exploration ability finds the promising region more early and then efficiently exploit the knowledge about the region to find the solution until exhaustion of the computational budget. Hence, overall, the supremacy of HLL-CMHS-sNDT is firmly established compared to other competing approaches, taking all performance indices into consideration.

C. Human Following Performance Evaluation

We also perform *four* experiments involving real motion in real scenarios to qualitatively evaluate the human following performance of HLL-CMHS-sNDT, by visual observation.

TABLE III

ASSESSMENT OF THE HUMAN FOLLOWING PERFORMANCE OF HLL-CMHS-sNDT

Experimental scenario	Path length traversed (in m)	Time taken for Completion (in min)	MAE (in m)		RMSE (in m)
			x	y	
Map1	13.01	3.88	0.0647	0.0655	0.0652
Map2	22.49	6.76	0.0681	0.0662	0.0673
Map3	21.11	6.44	0.0668	0.0657	0.0663
Map4	11.09	3.37	0.0629	0.0645	0.0636

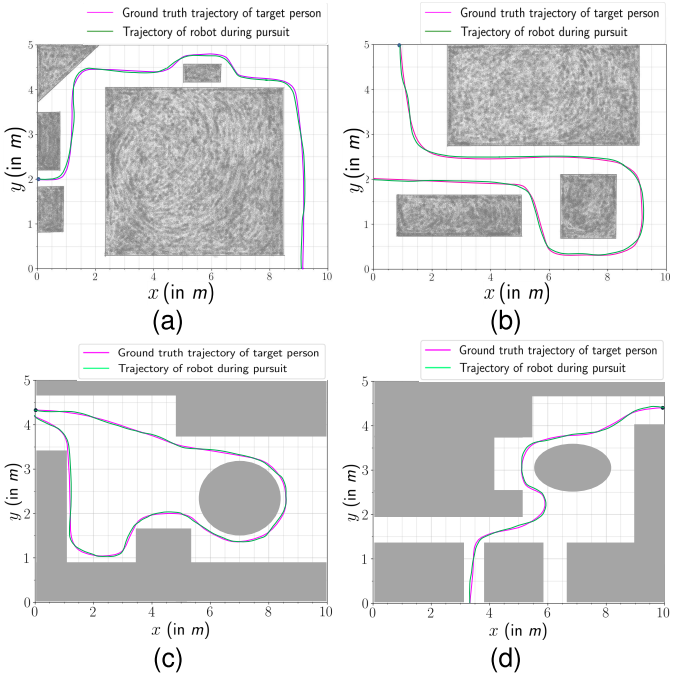

Fig. 9. Visual maps obtained during people following in four various real-life environments with our proposed HLL-CMHS-sNDT method: (a) Map1, (b) Map2, (c) Map3, and (d) Map 4. The *gray* areas indicate the spaces taken up by the stationary objects.

Results in Fig. 9 show that HLL-CMHS-sNDT is able to yield the human following results very close to the ground

truth maps. The corresponding quantitative results, obtained considering a corner in each experimental environment as the *reference point* with coordinates (0, 0), is given in Table III, which clearly demonstrates that the RMSEs and MAEs (in x-, y-directions), obtained between the points of the ground truth path and the path of the robot, are considerably small in comparison to the path lengths traversed.

VII. Conclusion

This work showed how metaheuristic-based search algorithms can be successfully utilized for solving sonar sensor-based HLL problems in human–robot coexisting environments. This approach is particularly useful in solving sonar scan matching algorithms suffering from bad initialization problems. The work also showed a successful real-life implementation of recently proposed DNLGSA for this purpose and proposed a new *CEDNLGSA* to achieve further improved performances. This novel HLL-CMHS-sNDT approach, when implemented in several real-life case studies, could, overall, sufficiently outperform various other state-of-the-art algorithms.

Acknowledgment

Prof. Sankar K. Pal acknowledges the National Science Chair, Science and Engineering Research Board, Department of Science and Technology (SERB-DST), Government of India.

References

[1] K. Kosuge and Y. Hirata, "Human–robot interaction," in *Proc. IEEE Int. Conf. Robot. Biomim.*, Shenyang, China, Aug. 2004, pp. 8–11.

[2] N. Najmaei, M. R. Kermani, and M. A. Al-Lawati, "A new sensory system for modeling and tracking humans within industrial work cells," *IEEE Trans. Instrum. Meas.*, vol. 60, no. 4, pp. 1227–1236, Apr. 2011.

[3] P. Paral, A. Chatterjee, and A. Rakshit, "OPTICS-based template matching for vision sensor-based shoe detection in human–robot coexisting environments," *IEEE Trans. Instrum. Meas.*, vol. 68, no. 11, pp. 4276–4284, Nov. 2019.

[4] P. Paral, A. Chatterjee, and A. Rakshit, "Chaos-based random sampling for photometric invariant shoe detection with vision sensor in human–robot coexisting environments," *IEEE Sensors J.*, vol. 20, no. 10, pp. 5424–5434, May 2020.

[5] J. Yuan, H. Chen, F. Sun, and Y. Huang, "Multisensor information fusion for people tracking with a mobile robot: A particle filtering approach," *IEEE Trans. Instrum. Meas.*, vol. 64, no. 9, pp. 2427–2442, Sep. 2015.

[6] P. Vadakkepat and L. Jing, "Improved particle filter in sensor fusion for tracking randomly moving object," *IEEE Trans. Instrum. Meas.*, vol. 55, no. 5, pp. 1823–1832, Oct. 2006.

[7] P. Paral, A. Chatterjee, and A. Rakshit, "Human position estimation based on filtered sonar scan matching: A novel localization approach using DENCLUE," *IEEE Sensors J.*, vol. 21, no. 6, pp. 8055–8064, Mar. 2021.

[8] A. Burguera, Y. González, and G. Oliver, "On the use of likelihood fields to perform sonar scan matching localization," *Auto. Robots*, vol. 26, no. 4, pp. 203–222, May 2009.

[9] P. Biber and W. Straßer, "The normal distributions transform: A new approach to laser scan matching," in *Proc. IEEE/RSJ Int. Conf. Intell. Robots Syst. (IROS)*, Las Vegas, NV, USA, Oct. 2003, pp. 2743–2748.

[10] D. Hähnell, W. Burgard, and S. Thrun, "Learning compact 3D models of indoor and outdoor environments with a mobile robot," *Robot. Auton. Syst.*, vol. 44, no. 1, pp. 15–27, Jul. 2003.

[11] I. Boussaïd, J. Lepagnot, and P. Siarry, "A survey on optimization metaheuristics," *Inf. Sci.*, vol. 237, pp. 82–117, Jul. 2013.

[12] Y. Wang, H.-X. Li, T. Huang, and L. Li, "Differential evolution based on covariance matrix learning and bimodal distribution parameter setting," *Appl. Soft. Comput.*, vol. 18, pp. 232–247, May 2014.

[13] L. Cui et al., "A novel artificial bee colony algorithm with depth-first search framework and elite-guided search equation," *Inf. Sci.*, vols. 367–368, pp. 1012–1044, Nov. 2016.

[14] W. T. Elsayed, Y. G. Hegazy, M. S. El-bages, and F. M. Bendary, "Improved random drift particle swarm optimization with self-adaptive mechanism for solving the power economic dispatch problem," *IEEE Trans. Ind. Informat.*, vol. 13, no. 3, pp. 1017–1026, Jun. 2017.

[15] N. Lynn and P. N. Suganthan, "Ensemble particle swarm optimizer," *Appl. Soft Comput.*, vol. 55, pp. 533–548, Jun. 2017.

[16] S. Mirjalili, S. M. Mirjalili, and A. Lewis, "Grey wolf optimizer," *Adv. Eng. Softw.*, vol. 69, pp. 46–61, Mar. 2014.

[17] S. Mirjalili and A. Lewis, "The whale optimization algorithm," *Adv. Eng. Softw.*, vol. 95, pp. 51–67, May 2016.

[18] E. Rashedi, H. Nezamabadi-Pour, and S. Saryazdi, "GSA: A gravitational search algorithm," *J. Inf. Sci.*, vol. 179, no. 13, pp. 2232–2248, Jun. 2009.

[19] S. Duman, U. Güvenç, Y. Sönmez, and N. Yörükeren, "Optimal power flow using gravitational search algorithm," *Energ. Convers. Manage.*, vol. 59, no. 59, pp. 86–95, Jul. 2012.

[20] S. Jiang, Y. Wang, and Z. Ji, "Convergence analysis and performance of an improved gravitational search algorithm," *Appl. Soft Comput.*, vol. 24, pp. 363–384, Nov. 2014.

[21] S. Mirjalili and A. Lewis, "Adaptive gbest-guided gravitational search algorithm," *Neural Comput. Appl.* vol. 25, nos. 7–8, pp. 1569–1584, Jun. 2014.

[22] A. Zhang, G. Sun, J. Ren, X. Li, Z. Wang, and X. Jia, "A dynamic neighborhood learning-based gravitational search algorithm," *IEEE Trans. Cybern.*, vol. 48, no. 1, pp. 436–447, Jan. 2018.

[23] *Python 2.7.16 Documentation Webpage*. Accessed: Sep. 30, 2019. [Online]. Available: https://docs.python.org/2.7/

[24] I. Petráš, *Fractional-Order Nonlinear Systems: Modeling, Analysis and Simulation*. Berlin, Germany: Springer-Verlag, 2011, pp. 7–184.

[25] H. Y. Jia, Z. Q. Chen, and G. Y. Qi, "Chaotic characteristics analysis and circuit implementation for a fractional-order system," *IEEE Trans. Circuits Syst. I, Reg. Papers*, vol. 61, no. 3, pp. 845–853, Mar. 2014.

[26] A. Burguera, Y. González, and G. Oliver, "A probabilistic framework for sonar scan matching localization," *Adv. Robot.*, vol. 22, no. 11, pp. 1223–1241, Jan. 2008.

[27] M. Ester, H.-P. Kriegel, J. Sander, and X. Xu, "A density-based algorithm for discovering clusters in large spatial databases with noise," in *Proc. 2nd Int. Conf. Knowl. Discovery Data Mining*, Portland, OR, USA, 1996, pp. 226–231.

[28] *Raspberry Pi 3 Model B+ Webpage*. Accessed: Mar. 10, 2021. [Online]. Available: https://www.raspberrypi.org/products/raspberry-pi-3-model-b-plus/

[29] *Camera Module—Raspberry Pi Documentation Webpage*. Accessed: Mar. 21, 2021. [Online]. Available: https://www.raspberrypi.org/documentation/hardware/camera/

[30] E. J. Morgan. (Nov. 16, 2014). *HC-SR04 Ultrasonic Sensor*. Accessed: Mar. 15, 2021. [Online]. Available: https://datasheetspdf.com/pdf/1380136/ETC/HC-SR04/1